www.springer.com/41230
https://doi.org/10.1007/s41230-026-4254-y
Research & Development
Vol. 23 No. 6 November 2026
CHINA FOUNDRY

# Microstructure and properties of Ti-Al-Sn-Zr-Mo-Nb-Ta-W-Si cast high-temperature titanium alloy

***Tian-yu Liu[1], Meng-fan Song[2], Cen-yang Wang[2], Hong-yu Liu[1], Wei-chen Qiu[1], and Shi-bing Liu[1]**

*1. State Key Laboratory of Advanced Casting Technologies, Shenyang Research Institute of Foundry Co., Ltd. CAM, Shenyang 110022, China*

*2. School of Materials Science and Engineering, Dalian University of Technology, Dalian 116024, Liaoning, China*

Copyright © 2026 Foundry Journal Agency

**Abstract:** A series of Ti-Al-Sn-Zr-Mo-Nb-Ta-W-Si high-temperature titanium alloy samples were designed and prepared with different $Mo_{eq}$ by a vacuum induction suspension melting furnace. The fluidity property, microstructure, and mechanical properties were investigated. Results show that the microstructures are composed of Widmanstätten structures, and the width of α-laths decreases from 2.85 μm to 1.43 μm as the addition of $Mo_{eq}$ increases from 0.86 to 4.48. It is also observed that with the increase of $Mo_{eq}$, the strength of the alloy increases at room temperature and decreases at 650 °C. Ti-5.76Al-2.30Sn-5.91Zr-3.10Mo-2.94Nb-1.16Ta-0.23Si alloy with the $Mo_{eq}$ of 4.16 exhibits a good combination of fluidity and mechanical properties at both room temperature and 650 °C, which is attributed to its minimum viscosity and maximum work hardening rate. This alloy can be considered a candidate material for casting high-temperature titanium alloys.

**Keywords:** high-temperature titanium alloy; casting property; microstructure; mechanical properties

**CLC numbers:** TG146.23 **Document code:** A **Article ID:** 1672-6421(2026)06-857-11

## 1 Introduction

In order to reduce noise and minimize fuel consumption in the aerospace industry, titanium alloys with high specific strength have become exceptionally attractive for aerospace applications[1, 2]. Compared to the β and (α+β) types, near-α titanium alloys, such as IMI685, IMI829, IMI834, Ti-1100, and Ti60 alloys, are widely used in jet engines as compressor disks and blades due to their high-temperature resistance and superior creep properties at elevated temperatures up to 600 °C[3]. The addition of multiple alloying elements is one of the most important ways to improve the high-temperature properties of titanium alloys[4]. Many researchers[5-8] have studied the effect of alloying elements, such as Zr, Mo, W, Nb, and Ta, on the microstructure and properties of high-temperature titanium alloys.

To meet the lightweight requirements of aero-engines, researchers have developed many high-temperature titanium alloys for service at 650 °C. Narayana et al.[9] designed a new alloy Ti-6.5Al-3.0Sn-4.0Hf-0.2Nb-0.4Mo-0.4Si-0.1B by replacing Zr with Hf. Compared to existing high-temperature titanium alloys, the new alloy showed higher mechanical properties at room temperature and 650 °C. Zhao et al.[10] developed a Ti-6.5Al-2Sn-4Zr-1.5Mo-2Nb-0.25Fe-0.2Si alloy with ultimate tensile strength of 575 MPa and elongation of 51.5% at 650 °C. Jayaprakash et al.[11] systematically investigated the effect of Zr and Si on the mechanical properties of near-α Ti-Al-Zr-Sn based alloys, the results showed that a higher content of Zr and Si can enhance the yield strength at 650 °C due to silicide precipitates.

Cluster-plus-glue-atom model is an efficient alloy composition design method for compositional design of titanium alloys. Jiang et al.[12] designed a Ti-Sn-Zr-Mo-Nb alloy by the cluster formula of $[(Mo_{0.5}Sn_{0.5})\text{-}(Ti_{13}Zr_1)]Nb_1$, which displays the lowest Young's modulus down to 48 GPa. Besides, Jiang et al.[13] designed a new series of alloys containing Mo/Ta/Nb elements by the cluster formula of $[Al\text{-}(Ti_{11.7}Zr_{0.3})](Ti_2Al_{0.69}Sn_{0.18}(Mo/Nb/Ta)_{0.03}Si_{0.1})$. They found that the alloys with the co-addition of Mo, Ta, and Nb have a high strength and good ductility at both room and high temperatures. Zhu et al.[14] designed a Ti-5.4Al-6.4Zr-6.2Sn-0.4Mo-1.6W-0.4Nb-3.2Ta-0.5Si alloy based on the cluster formula of $12[Al\text{-}Ti_{12}](AlTi_2)+5[Al\text{-}Ti_{12}Zr_2](Mo_{0.125}Nb_{0.125}Ta_{0.5}W_{0.25}Sn_{1.5}Si_{0.5})$, and the alloy achieved a strength level of 1 GPa at

***Tian-yu Liu**

Male, Ph. D. His research interests mainly focus on structural modeling of disordered materials, alloy design, and advanced manufacturing technology.

E-mail: liutianyusrif@163.com

**Received: 2024-11-23; Revised: 2025-03-17; Accepted: 2026-08-10**

600 °C in the as-cast state.

Currently, the studies of high-temperature titanium alloys mainly focus on the effect of alloying elements on microstructure and mechanical properties, and the effect on casting properties is still lacking. In this study, based on the cluster-plus-glue-atom model, a series of Ti-Al-Sn-Zr-Mo-Nb-Ta-W-Si alloys were developed by varying the elements (Mo, Nb, Ta, and W). The physical properties of these alloys with different $Mo_{eq}$ were calculated using the Thermo-Calc software, and the effects of these physical properties on the fluidity property were investigated. In addition, the effect of $Mo_{eq}$ on the microstructure and mechanical properties of high-temperature titanium alloys was also analyzed.

## 2 Experimental

In our previous work[14], the cluster formula of high-temperature titanium alloys, such as Ti65, IMI834, Ti-1100, was established, expressed as $12[Al\text{-}Ti_{12}](Al, Ti)_3+5[Al\text{-}(Ti, Zr)_{12}](Mo, Nb, Ta, W, Sn, Si)_3$. Based on the cluster formula, a series of Ti-Al-Zr-Mo-Nb-Ta-W-Si high-temperature titanium alloys was designed by adjusting the proportion of alloying elements. Table 1 shows the measured composition and Mo equivalent ($Mo_{eq}$) of the designed alloys. The $Mo_{eq}$ can indicate the β-stabilizing effect of the addition of different elements on titanium alloy, and can be calculated via the $Mo_{eq}$ equation[15]:

$$Mo_{eq}=1.0\%Mo+0.2\%Ta+0.28\%Nb+0.4\%W+0.67\%V+1.25\%Cr+1.25\%Ni+1.7\%Mn+1.7\%Co+2.5\%Fe \quad (1)$$

The designed alloys (about 12 kg) were prepared by a vacuum induction suspension melting furnace, and were melted three times to ensure the homogeneity of alloy composition. Then poured into the spiral graphite mold, as shown in Fig. 1. In order to eliminate the influence of the melting process and casting conditions on the fluidity properties of these alloys, the same melting process and casting conditions were used. Three spiral samples for each alloy composition were prepared.

The samples for microstructure and mechanical properties analysis were taken from the spiral sample runner, as shown in Fig. 1(a), and each alloy was selected at the same position. In order to eliminate defects such as shrinkage and porosity, the spiral samples were then subjected to hot isostatic pressing (HIP) with a scheme of 920 °C/125 MPa/2 h after measuring their flow length.

Microstructure was observed via optical microscopy (OM, ZEISS Axio Ver. A1) and scanning electron microscopy (SEM, ZEISS EVO MA25) with a Kroll reagent (1 mL HF, 3 mL $HNO_3$, and 50 mL $H_2O$). The size of α phases was measured in OM and SEM morphology images (at least 6 images) by using the Image-Pro Plus 6.0 software.

The micro-hardness tests of all the alloys under different $Mo_{eq}$ were performed using a Wilson VH1150 apparatus with a load of 10 kg for 12 s, where each alloy was conducted at

**Table 1: Measured composition (wt.%) and $Mo_{eq}$ of designed alloys**

| Alloys | Ti | Al | Sn | Zr | Mo | Nb | Ta | W | Si | $Mo_{eq}$ |
|---|---|---|---|---|---|---|---|---|---|---|
| 1 | 83.05 | 6.16 | 2.56 | 6.68 | 0.68 | 0.64 | 0 | 0 | 0.23 | 0.86 |
| 2 | 80.38 | 5.86 | 2.40 | 6.14 | 0.65 | 1.85 | 1.21 | 1.23 | 0.28 | 1.90 |
| 3 | 77.27 | 5.73 | 2.31 | 6.02 | 0.61 | 2.98 | 2.35 | 2.38 | 0.35 | 2.87 |
| 4 | 78.28 | 5.94 | 2.50 | 6.36 | 2.07 | 1.97 | 2.46 | 0 | 0.42 | 3.11 |
| 5 | 78.58 | 5.88 | 2.49 | 6.30 | 2.04 | 0.66 | 1.22 | 2.49 | 0.34 | 3.46 |
| 6 | 78.80 | 5.95 | 2.50 | 5.92 | 2.06 | 3.27 | 0 | 1.24 | 0.26 | 3.47 |
| 7 | 78.60 | 5.76 | 2.30 | 5.91 | 3.10 | 2.94 | 1.16 | 0 | 0.23 | 4.16 |
| 8 | 77.76 | 5.79 | 2.44 | 6.22 | 3.35 | 0.65 | 2.42 | 0.95 | 0.42 | 4.40 |
| 9 | 78.33 | 5.92 | 2.51 | 6.33 | 3.43 | 1.95 | 0 | 1.26 | 0.27 | 4.48 |

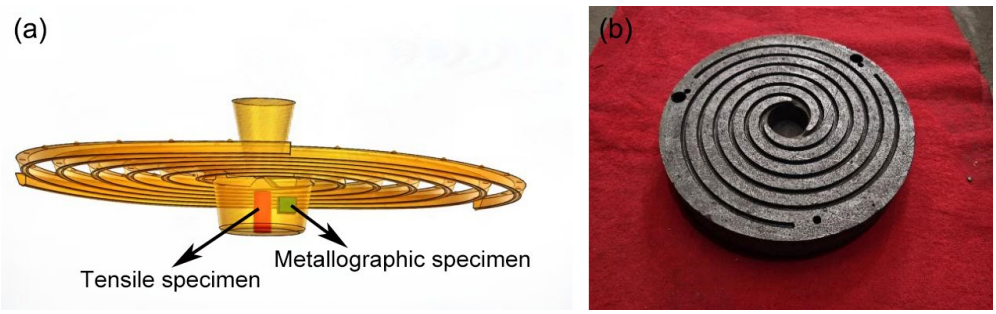



**Fig. 1: Model of spiral specimen and schematic diagram of sampling positions for tensile specimens and metallographic specimens (a) and physical picture of spiral graphite mold (b)**

least five times. Uniaxial tensile tests at room temperature and 650 °C were performed on an E45 with a strain rate of $1\times10^{-3}$. The dimensions of tensile specimens are shown in Fig. 2.

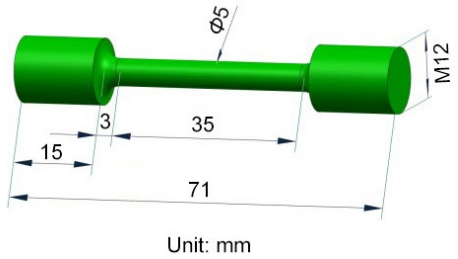



**Fig. 2: Size of tensile test samples at room temperature and 650 °C**

# 3 Results and discussion

## 3.1 Fluidity property

Figure 3 shows the images of spiral samples of different alloys under different $Mo_{eq}$, and Fig. 4 displays the changes in the length of spiral samples under different $Mo_{eq}$. According to Figs. 3 and 4, as $Mo_{eq}$ increases from 0.86 to 3.47, the length of the spiral specimen decreases from 43 cm to 34 cm. However, with the further increase in $Mo_{eq}$, the length of the spiral specimen increases. Among them, when $Mo_{eq}$ equals 4.16, the length of the spiral specimen reaches 44 cm, which is the longest distance among all the alloys. The results show that Ti-5.76Al-2.30Sn-5.91Zr-3.10Mo-2.94Nb-1.16Ta-0.23Si alloy has excellent casting performance.

In general, the fluidity of the alloy improves with decreasing viscosity. Figure 5 shows the changes in the kinematic viscosity of the alloys under different $Mo_{eq}$ calculated via Thermo-Calc software. The result shows that the kinematic viscosity decreases from $7.51\times10^{-7}$ $m^2\cdot s^{-1}$ to $6.95\times10^{-7}$ $m^2\cdot s^{-1}$ with increasing $Mo_{eq}$ from 0.86 to 4.16, and then increases from $7.00\times10^{-7}$ $m^2\cdot s^{-1}$ to $7.20\times10^{-7}$ $m^2\cdot s^{-1}$ with increasing $Mo_{eq}$ from 4.40 to 4.48. Thus, the alloy with a $Mo_{eq}$ of 4.16 possesses the lowest viscosity, which indicates the highest fluidity. Nevertheless, when $Mo_{eq}$ is 0.86, the alloy shows high fluidity despite of its high viscosity. This suggests the involvement of other contributing factors.

Furthermore, the variation in thermal capacity of the alloy using Thermo-Calc software was calculated, as shown in Fig. 6. Obviously, the thermal capacity decreases from 499.34 $J\cdot K^{-1}$ to 262.06 $J\cdot K^{-1}$ with increasing $Mo_{eq}$ from 0.86 to 4.48. Heat capacity is a critical factor for alloy fluidity[16]. A higher heat capacity is associated with improved fluidity. This explains that the alloy with $Mo_{eq}$=0.86, despite of its high viscosity, demonstrates high fluidity.

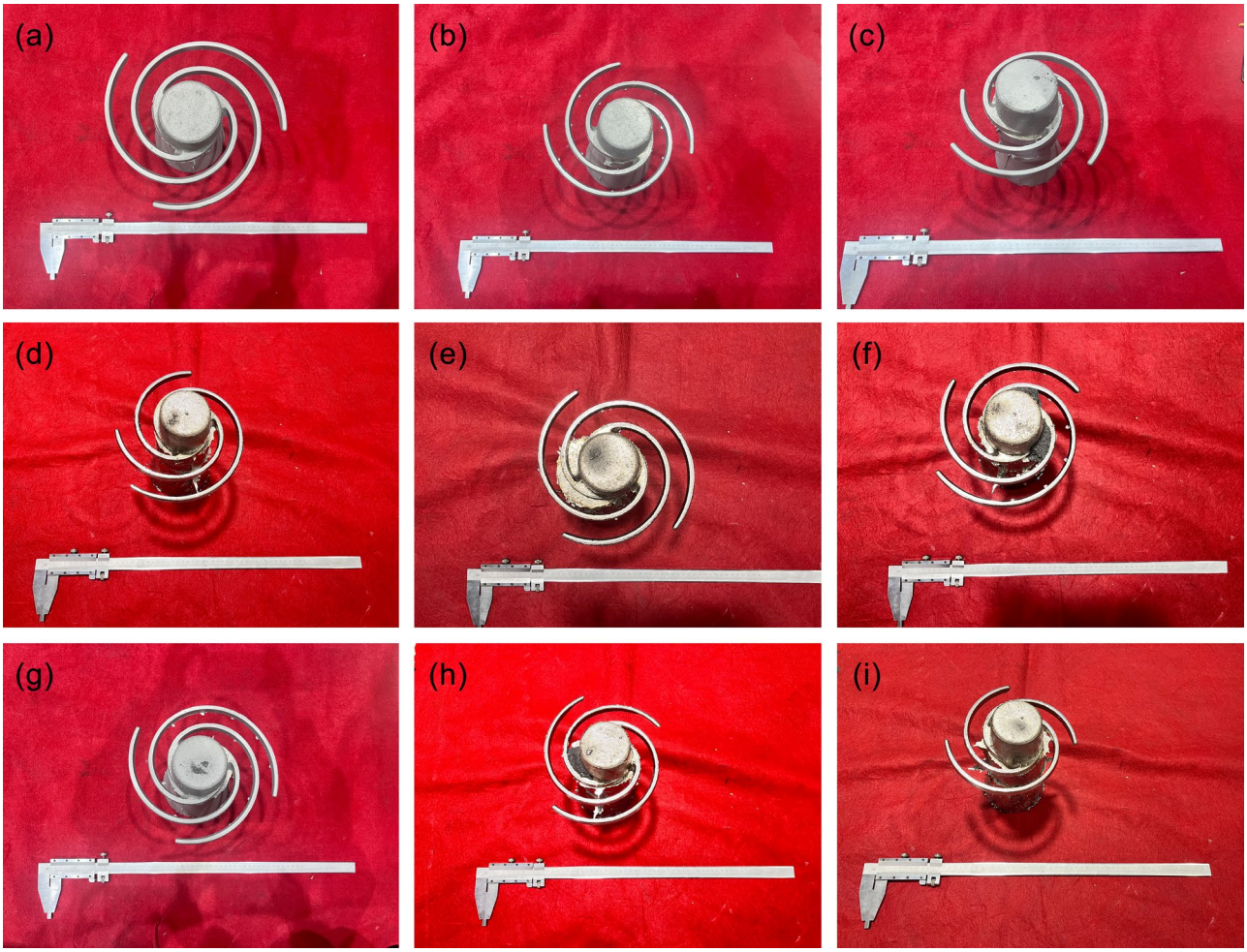



**Fig. 3: Images of spiral samples with different $Mo_{eq}$: (a) $Mo_{eq}$=0.86; (b) $Mo_{eq}$=1.90; (c) $Mo_{eq}$=2.87; (d) $Mo_{eq}$=3.11; (e) $Mo_{eq}$=3.46; (f) $Mo_{eq}$=3.47; (g) $Mo_{eq}$=4.16; (h) $Mo_{eq}$=4.40; (i) $Mo_{eq}$=4.48**

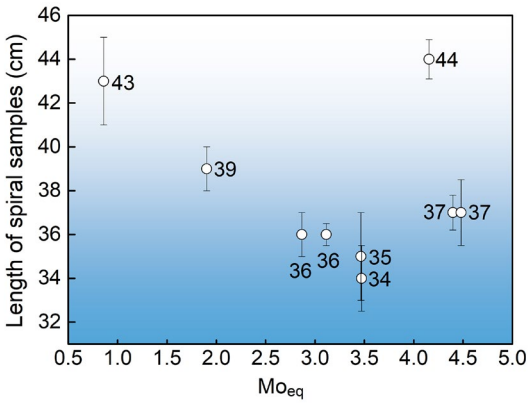



Fig. 4: Changes in length of spiral samples with different Mo$_{eq}$

## 3.2 Microstructure and mechanical properties

Figures 7(a, b, c) show the XRD spectra of Ti-Al-Sn-Zr-Mo-Nb-Ta-W-Si alloys with different Mo$_{eq}$. It can be seen that there are α and β phases diffraction peaks in all the alloys with different Mo$_{eq}$, indicating that the designed Ti-Al-Sn-Zr-Mo-Nb-Ta-W-Si alloys are composed of α+β phases. Based on the XRD spectra, the content of β phase with different Mo$_{eq}$ was calculated. As the Mo$_{eq}$ increases from 0.86 to 4.48, the β-phase content increases from 3.7% to 24.9%, as shown in Fig. 7(d).

Figure 8 displays the OM images of the alloys with different Mo$_{eq}$. The results show that the microstructure characteristics

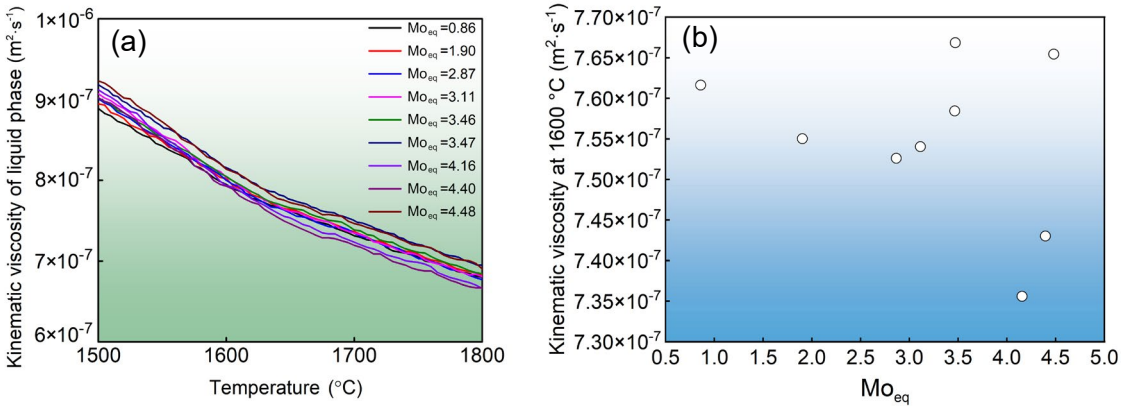



Fig. 5: Changes in kinematic viscosity of alloys under different Mo$_{eq}$ calculated via Thermo-Calc software: (a) curves of kinematic viscosity with temperature; (b) kinematic viscosity in liquid metal

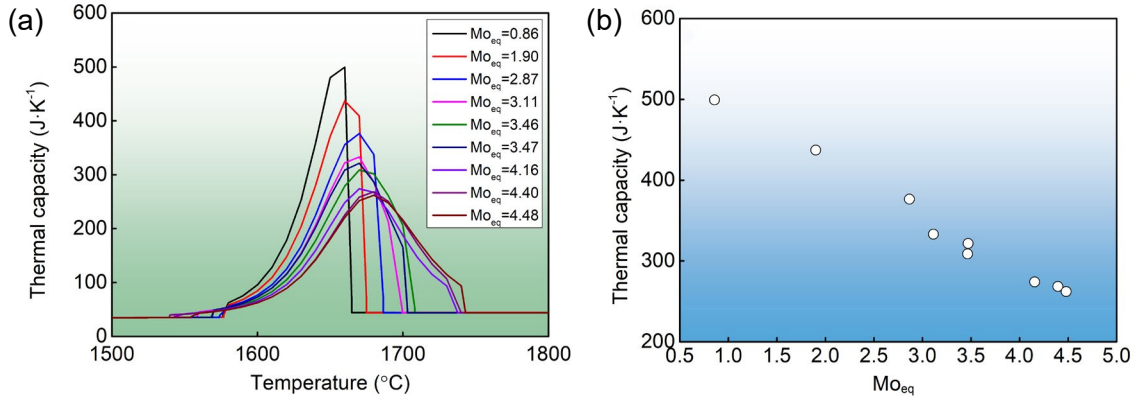



Fig. 6: Changes in thermal capacity of alloys under different Mo$_{eq}$ calculated via Thermo-Calc software: (a) change curves of thermal capacity; (b) changes in thermal capacity of alloys under different Mo$_{eq}$

do not show much difference. The microstructure is composed of Widmanstätten structures. Besides, a multitude of individual α-laths are separated by a thin layer of retained β phase, as shown in Fig. 9. The effects of the width of α-laths can be deduced from these images, as shown in Fig. 10. The width of α-laths varies from 2.85 μm to 1.43 μm with the increase of Mo$_{eq}$ from 0.86 to 4.48. As solute elements, Mo, Nb, Ta, and W can affect the nucleation and growth processes of α-laths. The nucleation rate ($N$) of the α phase in the undercooled melt can be described as Eq. (2)[17]:

$$N=K_v\exp(-\Delta G_k/kT)\exp(-\Delta G_A/kT) \quad (2)$$

where $K_v$ is constant, $\Delta G_k$ is the nucleation energy, $k$ is boltzmann constant, $T$ is absolute temperature, and $\Delta G_A$ is the activation energy of the transfer of atoms from the liquid to the nuclei. The nucleation energy of the new phase, $\Delta G_k$, is expressed as Eq. (3)[18]:

$$\Delta G_k=16\pi\sigma_3 T_m/[3(L_m\cdot\Delta T)]^2 \quad (3)$$

As surface-active substances, Mo, Nb, Ta, and W can reduce the interfacial energy, which will decrease the nucleation energy $\Delta G_k$. Therefore, increasing the content of Mo, Nb, Ta, and W can improve the nucleation rate $N$, which decreases the width of α-laths. In addition, the enrichment of β-stabilizing elements, including Mo, Nb, Ta, and W in β phase, raises β phase content. Consequently, the increased β phase content can hinder the movement of grain boundaries to reduce the width of α-laths.

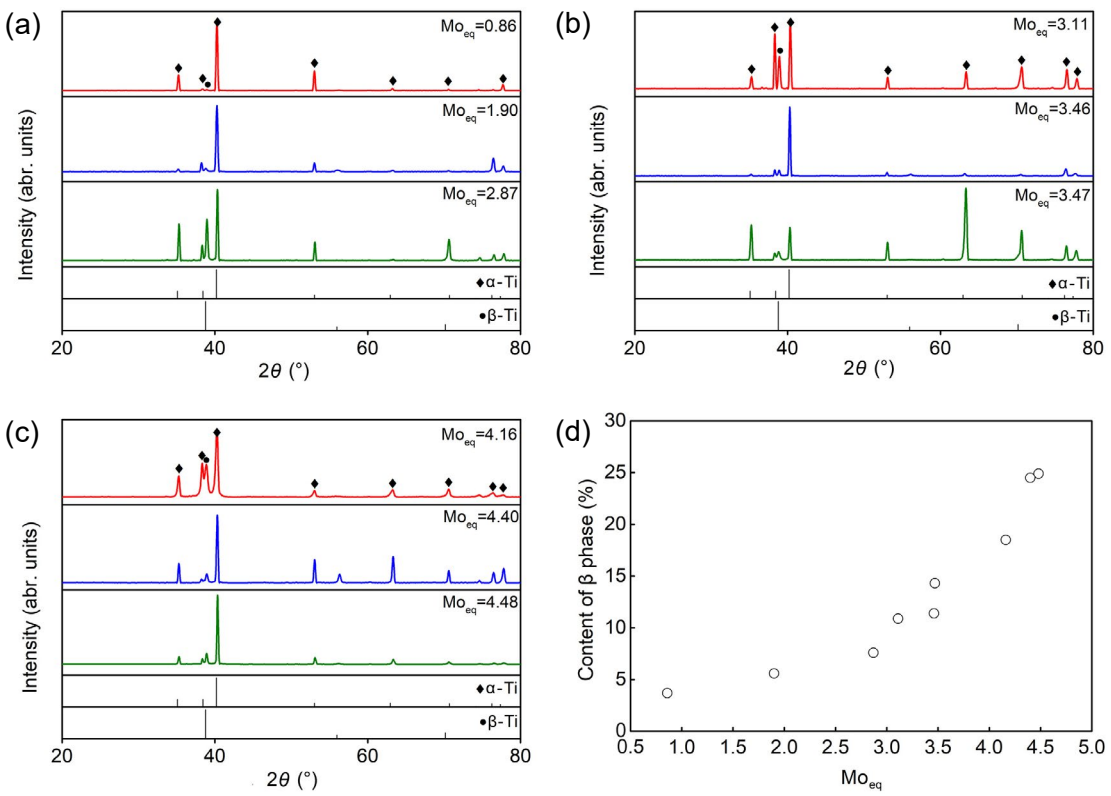



Fig. 7: XRD spectra of alloys with different $Mo_{eq}$ (a, b, c) and the content of β phase with different $Mo_{eq}$ (d)

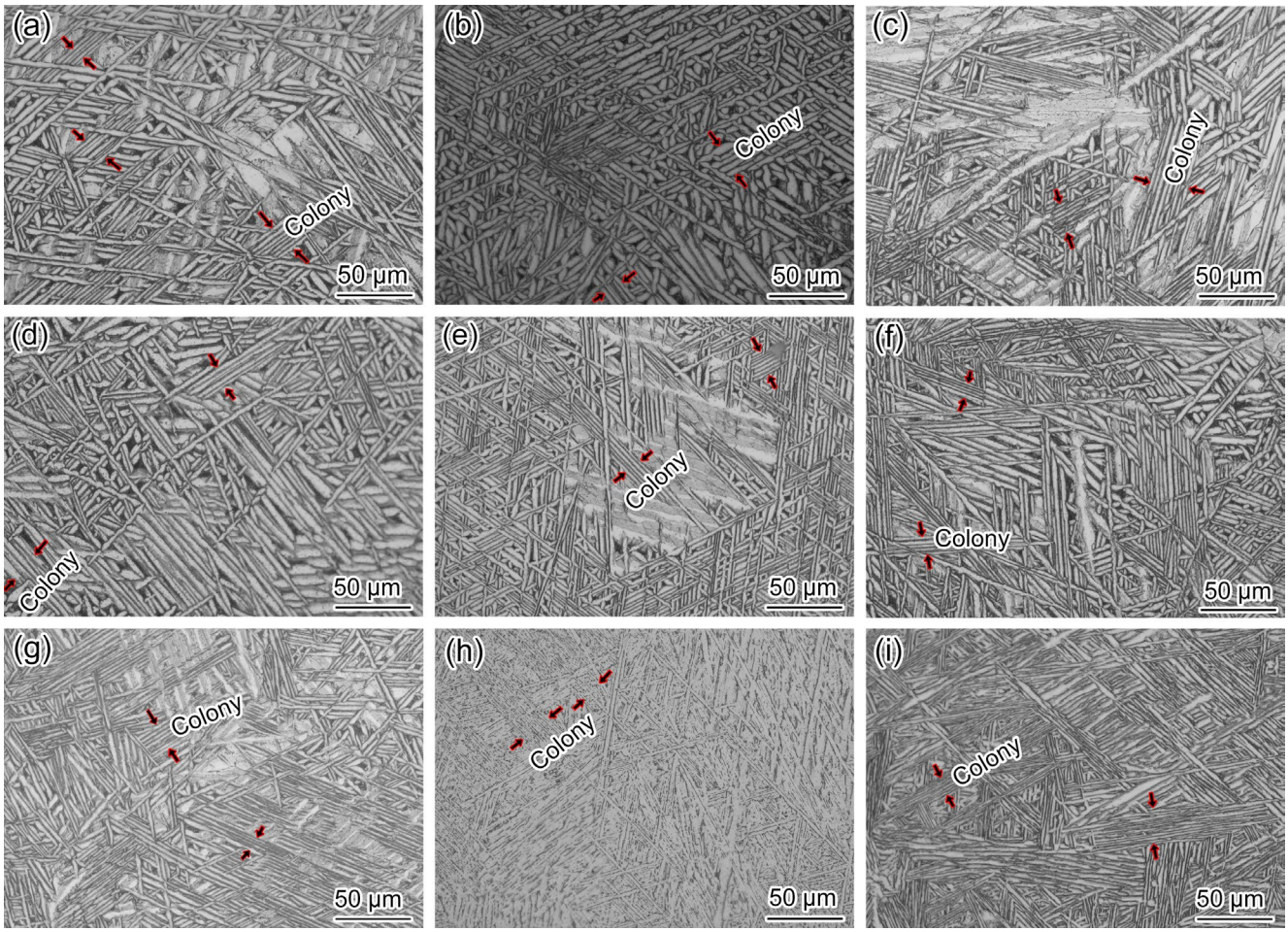



Fig. 8: OM images of alloys with different $Mo_{eq}$: (a) $Mo_{eq}$=0.86; (b) $Mo_{eq}$=1.90; (c) $Mo_{eq}$=2.87; (d) $Mo_{eq}$=3.11; (e) $Mo_{eq}$=3.46; (f) $Mo_{eq}$=3.47; (g) $Mo_{eq}$=4.16; (h) $Mo_{eq}$=4.40; (i) $Mo_{eq}$=4.48

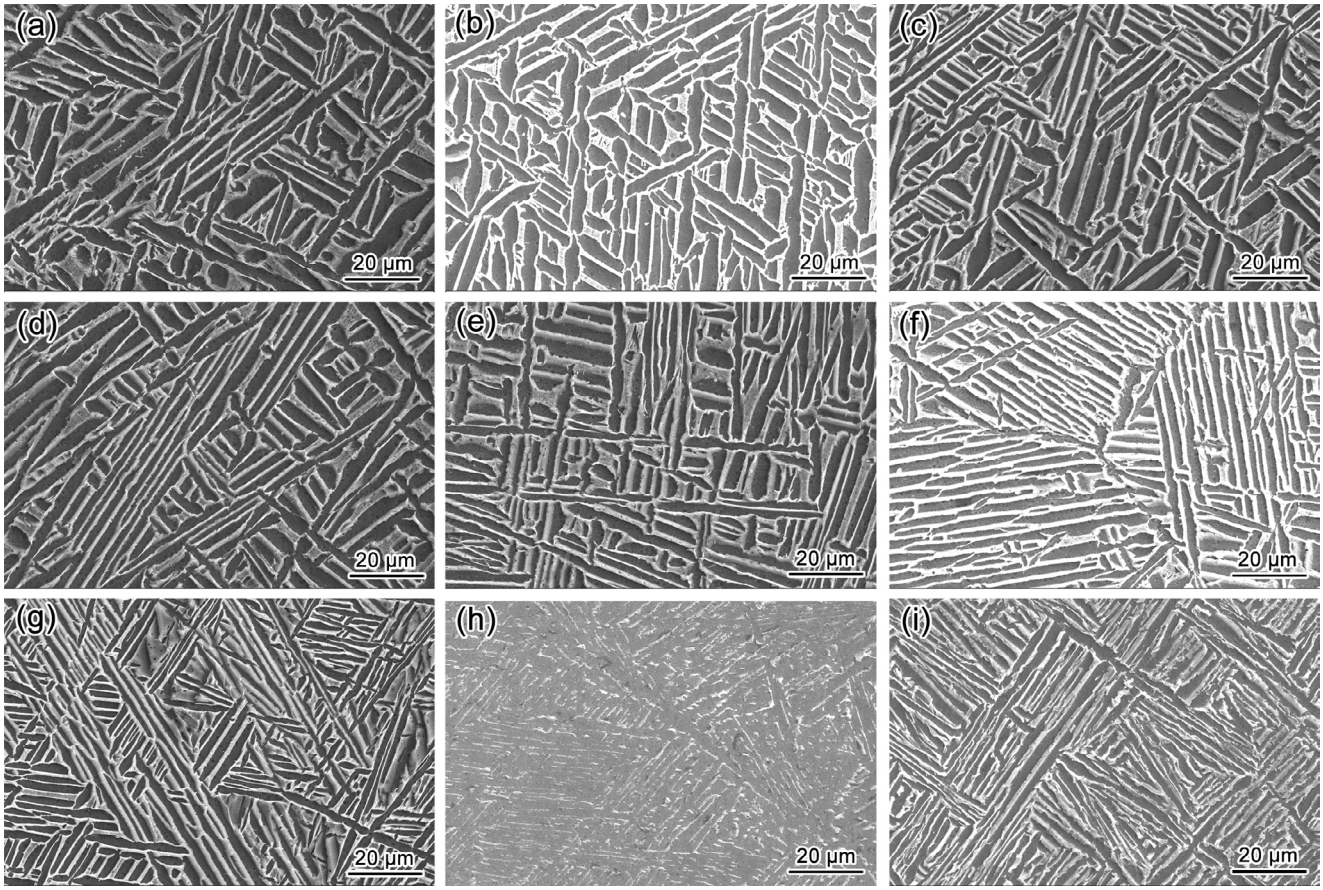



**Fig. 9: SEM images of alloys with different $Mo_{eq}$: (a) $Mo_{eq}$=0.86; (b) $Mo_{eq}$=1.90; (c) $Mo_{eq}$=2.87; (d) $Mo_{eq}$=3.11; (e) $Mo_{eq}$=3.46; (f) $Mo_{eq}$=3.47; (g) $Mo_{eq}$=4.16; (h) $Mo_{eq}$=4.40; (i) $Mo_{eq}$=4.48**

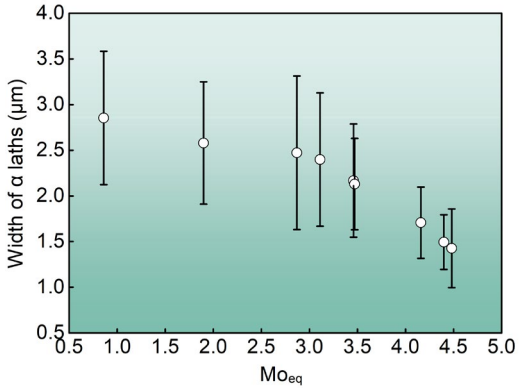



**Fig. 10: Changes in grain size of alloys with different $Mo_{eq}$**

Figures 11 through 13 show the texture for the alloy with different $Mo_{eq}$. As can be seen from these figures, the phase constitution and grain morphology exhibit obviously regular changes as $Mo_{eq}$ increases. The inverse pole figure (IPF) of low-$Mo_{eq}$ alloys ($Mo_{eq}$≤2.87) [Figs. 11(a, d, g)] shows that the microstructure is dominated by a typical Widmanstätten/basket-weave α phase. A large amount of acicular/lamellar α phase precipitates within coarse primary β grains, forming an interwoven lamellar bundle, and the orientation distribution of the lamellar α phase exhibits significant anisotropy. When the β→α phase transformation occurs during cooling, the α phase precipitates along specific habit planes within the β grains, forming a lamellar structure with Burgers orientation relationships.

Furthermore, in low-$Mo_{eq}$ alloys, the {0001}α polar graph exhibits obvious textural characteristics, with a maximum pole density as high as 24.6. The pole density distribution shows a significant tendency to concentrate along specific directions, reflecting a pronounced preference for the *c*-axis orientation of the lamellar α phase, which is directly related to the selection effect of α phase variants under the Burgers orientation relationship. The pole figure distributions for the {11-20}α and {10-10}α phases are relatively dispersed, but still exhibit some orientation concentration, with the overall texture intensity remaining at a high level, as shown in Figs. 11(c, f, i).

As $Mo_{eq}$ increases to the intermediate range (3.11≤$Mo_{eq}$≤ 3.47), the IPFs [Figs. 12(a, d, g)] show that the original β grain size gradually increases, the volume fraction of the lamellar α phase within the grains decreases significantly, and the aspect ratio decreases, block/equiaxial α phases appear in some regions, and microstructural uniformity improves. At the same time, changes in the IPF color distribution indicate a reduction in the orientation diversity of the α phase and in the orientation difference within some lamellar bundles, reflecting the inhibitory effect of increased β-phase stability on the kinetics of the α-phase transformation, which weakens the variant selection effect during α-phase precipitation.

Besides, as $Mo_{eq}$ increases to an intermediate level, the uniformity of the pole density distribution improves significantly. This change is directly related to the reduced layering of the α phase and the increased tendency toward

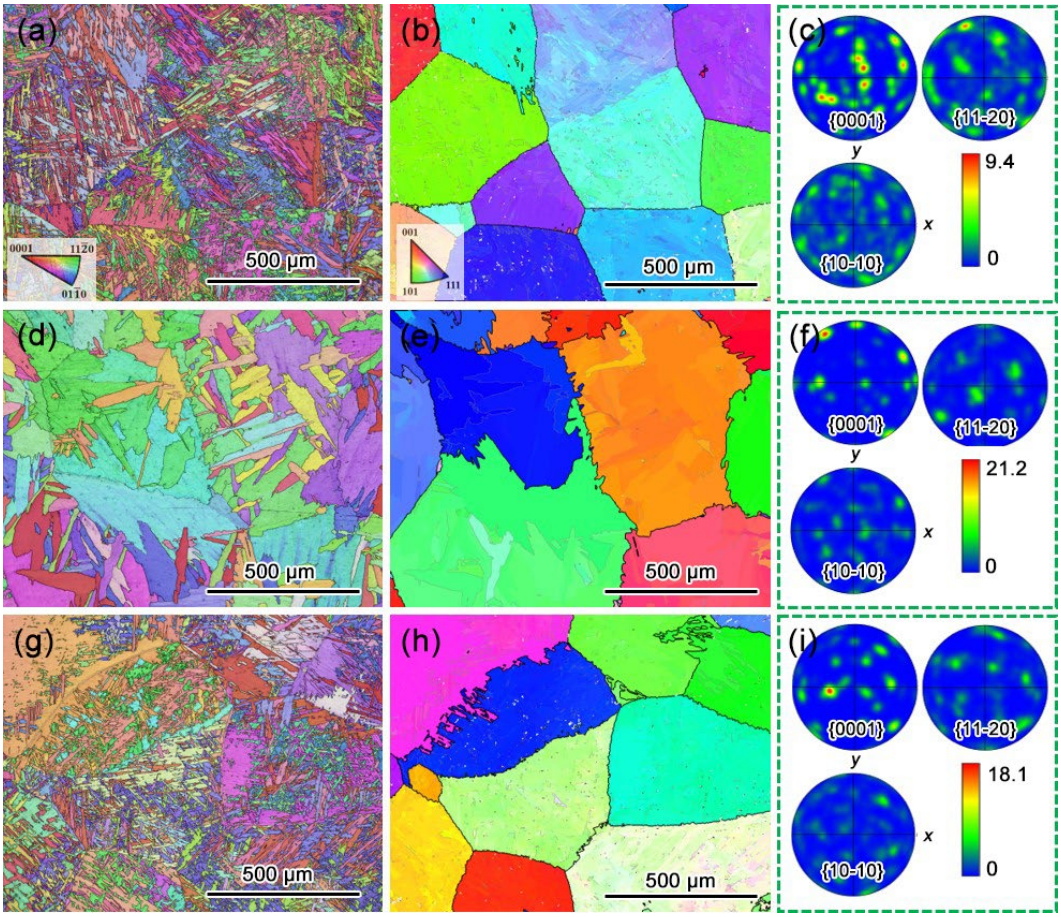



Fig. 11: IPF, grain orientation maps, and PF of alloys at different $Mo_{eq}$: (a–c) $Mo_{eq}$=0.86; (d–f) $Mo_{eq}$=1.90; (g–i) $Mo_{eq}$=2.87

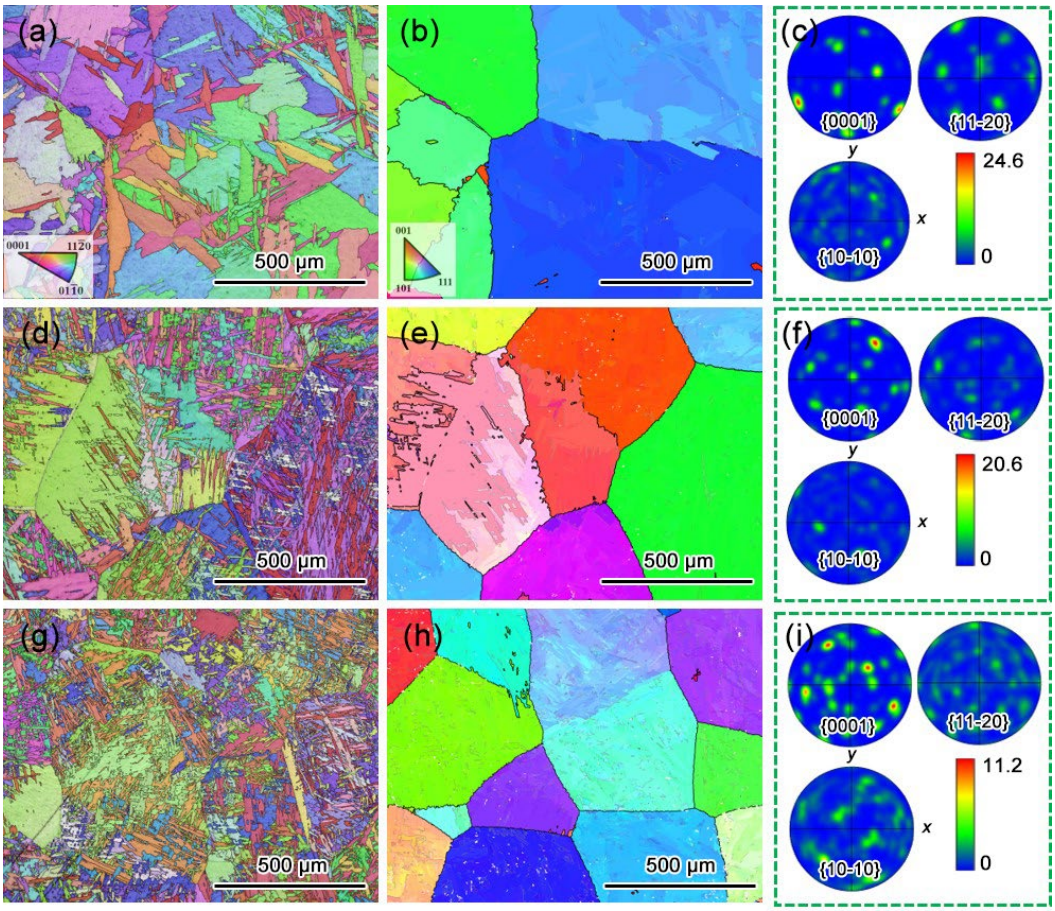



Fig. 12: IPF, grain orientation maps, and PF of alloys at different $Mo_{eq}$: (a–c) $Mo_{eq}$=3.11; (d–f) $Mo_{eq}$=3.46; (g–i) $Mo_{eq}$=3.47

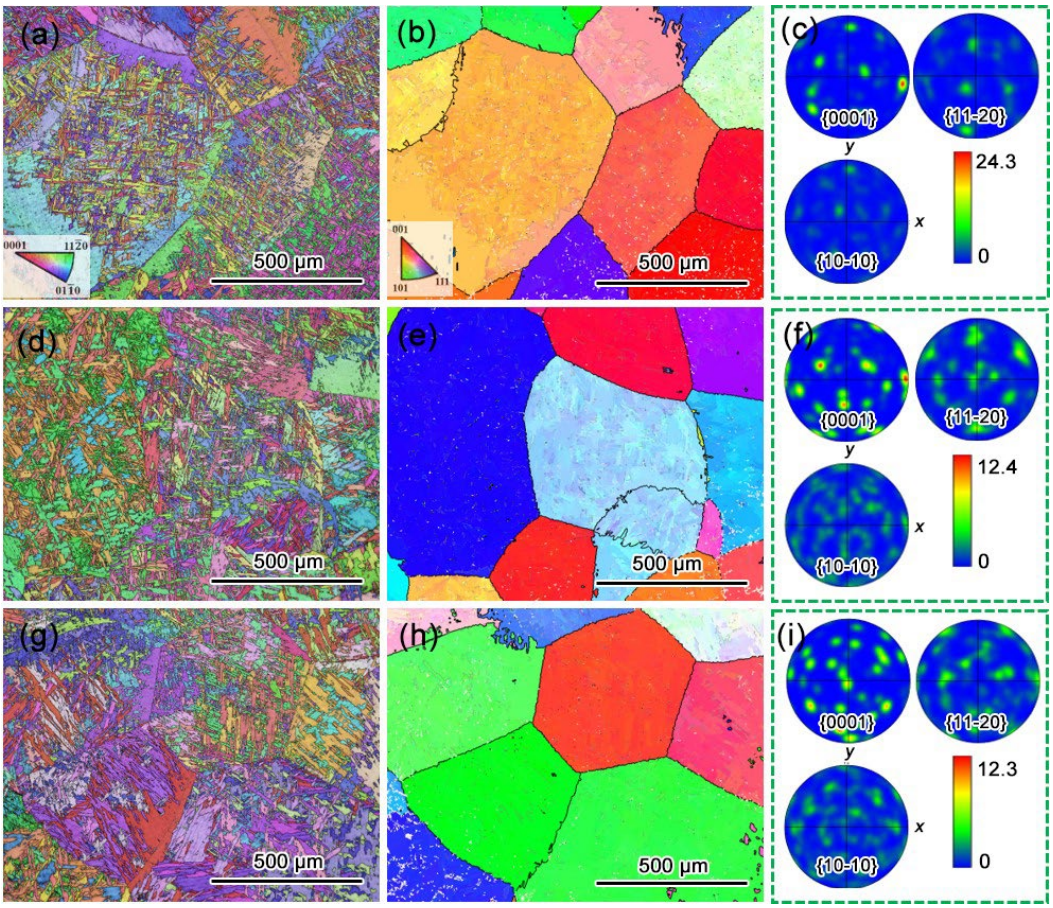



**Fig. 13: IPF, grain orientation maps, and PF of alloys at different $Mo_{eq}$: (a–c) $Mo_{eq}$=4.16; (d–f) $Mo_{eq}$=4.40; (g–i) $Mo_{eq}$=4.48**

isotropic alignment; the weakening of the variant selection effect has made the orientation distribution of the α phase more random, as shown in Figs. 12(c, f, i).

As $Mo_{eq}$ further increases ($Mo_{eq}$≥4.16), the isometric/block α phase becomes the predominant morphology, and the continuous α phase film at original β grain boundaries gradually disappears. Besides, the grain boundary features tend to become straight. With the high $Mo_{eq}$, the stability of the β phase increases significantly, and the phase transformation driving force decreases, which inhibits the lamellar precipitation of the α phase and promotes the formation of the equiaxed α phase.

In high-$Mo_{eq}$ alloys, the pole density distribution exhibits a multi-peak and homogenized characteristics, with no obvious strong textural orientations. This indicates that the precipitation behavior of the α phase tends toward isotropy at high $Mo_{eq}$, and the crystallographic texture is significantly weakened. At the same time, the pole density distributions of the {11-20}α and {10-10}α pole figures also tend toward uniformity, with texture intensity decreasing to its lowest level, as shown in Figs. 13(c, f, i).

Figure 14 shows the average micro-hardness of alloys with different $Mo_{eq}$. The average micro-hardness increases from 329 HV to 362 HV with the increase of $Mo_{eq}$ from 0.86 to 4.48. According to the work by Devaraj et al[18], the strength is related to the grain size:

$$\sigma \propto K_P/l_P+K_S/l_S \quad (4)$$

where $\sigma$ is the strength, $K_P$ and $K_S$ are Taylor factor constants, and $l_P$ and $l_S$ are the inter-particle spacing of primary and secondary α phases, respectively. In this study, secondary α phases are not found. Thus, the changes in micro-hardness can be attributed to the primary α. According to Eq. (3), the finer α-laths lead to a reduction in the average distance between the dislocations from the adjacent α-laths, which enhances the strength. The finer α-laths also decrease the dislocation glide length to improve the strength[19].

Figure 15 shows the tensile strength and elongation of alloys with different $Mo_{eq}$ obtained at room temperature by tensile testing. The elongation decreases from 10% to 7.5% with increasing $Mo_{eq}$ from 0.86 to 2.87. But the alloy with $Mo_{eq}$=3.11 exhibits the highest elongation, 10.5%. Then, elongation decreases from 10% to 7% with $Mo_{eq}$ increasing from 3.46 to 4.48.

In the low $Mo_{eq}$ range, the content of β-stabilizing elements is relatively low, resulting in weaker drag and pinning effects on α-phase growth. The α phase tends to grow epitaxially along specific habit planes, forming a well-ordered large Widmanstätten structure. Corresponding polar graph analysis shows that under these conditions, the α phase exhibits a very obvious {0001} basal plane texture, while the β phase also displays preferential orientation, with highly consistent grain orientation. This obvious texture, combined with the coarse lamellar structure, results in relatively simple dislocation slip paths and low slip resistance, causing the alloy to exhibit low

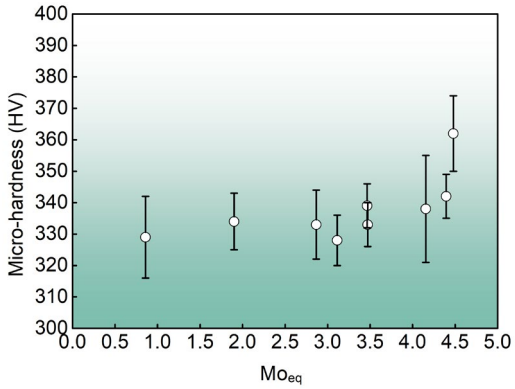



Fig. 14: Changes in micro-hardness of alloys with different $Mo_{eq}$

strength (approximately 958 MPa), high ductility (reduction of area approximately 14%), and high anisotropy. As $Mo_{eq}$ continues to increase, the solid solution content of β-stabilizing elements such as Mo, Nb, Ta, and W increases significantly. These elements produce a strong drag effect at grain boundaries and phase boundaries, effectively reducing the width of the α lamellae (from approximately 2.85 μm to less than 1.43 μm), while simultaneously disrupting the oriented growth pattern of the α phase, leading to a significant weakening of the texture strength and a transition from an obvious basal-plane texture to a nearly random texture. Polar graph data indicate that, at high $Mo_{eq}$, the texture peaks transform from sharp, point-like features to a diffuse distribution, and the orientation of the α/β phases tends toward isotropy. This weakening of texture, plus the refinement of the α lamellae, collectively forms a high-density network of α/β phase boundaries and dislocation barriers. The evolution of microstructure and texture directly drives the significant improvement in room-temperature mechanical properties: on the one hand, the refinement of α lamellae enhances the grain refinement effect, while the high-density phase boundaries provide high resistance to dislocation slip; on the other hand, the weakening of texture improves the material's isotropy, further enhancing its resistance to deformation. In addition, the solid solution strengthening effect produced by high concentrations of β-stabilizing elements in the β phase combines with the aforementioned microstructural strengthening mechanisms, ultimately increasing the alloy's tensile strength and yield strength from approximately 958 MPa and 842 MPa to 1,065 MPa and 952 MPa, respectively. It is worth noting that, except the significant increase in strength, the high-$Mo_{eq}$ alloy still retains an elongation of approximately 7.5% and a reduction of area of 10%. This is because the fine and multidirectionally interlaced basket-weave microstructure effectively deflects crack propagation paths and alleviates stress concentration, thereby maintaining great plasticity while ensuring high strengthening.

Figure 16 shows the work hardening rate curves for the alloys with different $Mo_{eq}$. The results indicate that the work-hardening rate curves of all alloys display multi-stage work-hardening behavior. In the early stage of deformation, the work-hardening rate of all alloys sharply decreases. Then, the drop in work hardening rate is suppressed, and the $Mo_{eq}$ has a remarkable effect on the work hardening. When

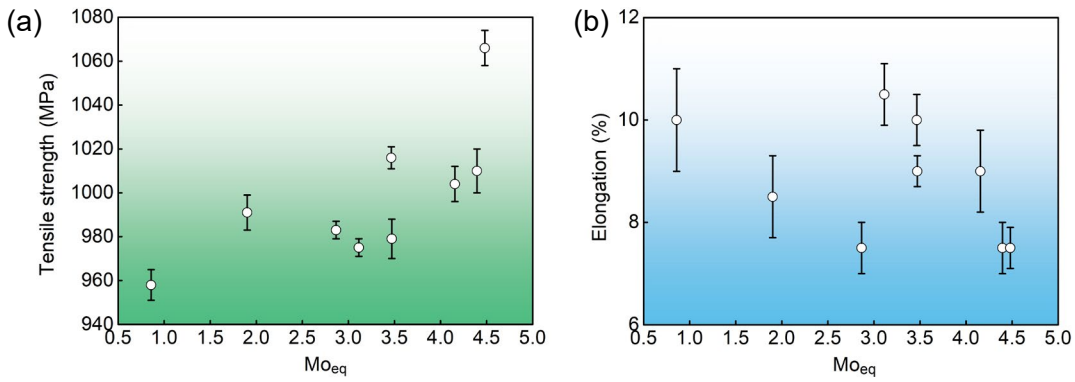



Fig. 15: Changes in tensile strength and elongation of alloys under different $Mo_{eq}$ obtained at room temperature by tensile test: (a) tensile strength; (b) elongation

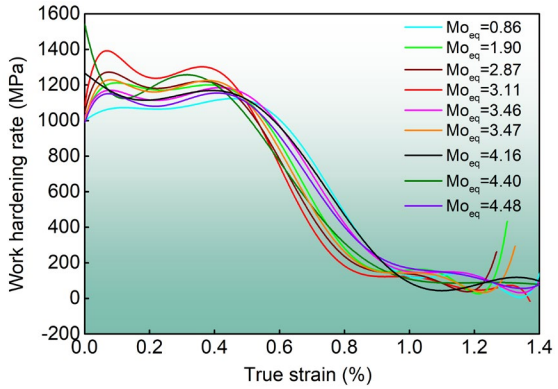



Fig. 16: Changes in work hardening rate of alloys with different $Mo_{eq}$

$0.86 \le Mo_{eq} \le 2.87$ or $Mo_{eq} \ge 4.40$, the work hardening rate slightly increases with the increase of strain. But for the $Mo_{eq}$ between 3.11 and 4.16, the work hardening rate increases, which indicates these alloys have higher work hardening capacity with improved strength and elongation[20].

Figure 17 shows the tensile strength and elongation of alloys under different $Mo_{eq}$ obtained at 650 °C. It can be seen that the strength decreases from 582 MPa to 522 MPa as $Mo_{eq}$ increases from 0.86 to 4.48, while the elongation increases from 5.6% to 12.5%. At high temperatures, compared with the α phase, the β phase is soft. With the increase of $Mo_{eq}$, the content of the β phase rises, resulting in the decrease of strength and the increase of elongation.

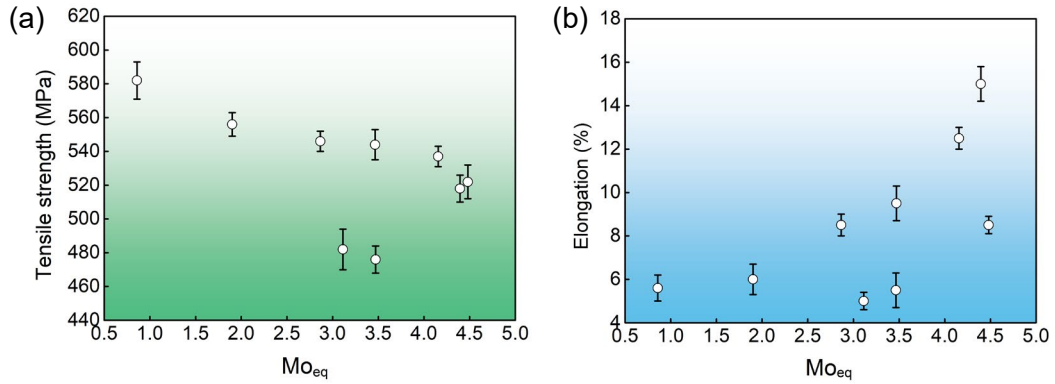



**Fig. 17: Changes in tensile strength and elongation of alloys with different $Mo_{eq}$ obtained at 650 °C by tensile testing: (a) tensile strength; (b) elongation**

The evolution of high-temperature mechanical properties is closely relevant to the alloy composition, microstructure, and crystallographic texture. In the low $Mo_{eq}$ range, the content of β-stabilizing elements is low, resulting in limited inhibition of α-phase growth. The α phase grows along specific habit planes within β grains, forming a coarse-grained α-strip bundle structure with highly consistent orientation. According to the corresponding polar graph analysis, under these conditions, the α phase exhibits extremely strong {0001} basal plane texture, while the β phase also displays significant preferential orientation. This structure consisting of coarse lamellae and a strong texture has a dual effect at high temperatures: on the one hand, the coarse α lamellae have a low phase boundary density and weak resistance to dislocation slip; however, the unidirectional growth of the α phase effectively hinders grain boundary sliding and dislocation climb at high temperatures due to the coarse bundles. At the same time, the low β-phase content results in a high intrinsic strength of the alloy matrix, leading to the highest high-temperature tensile strength (approximately 580 MPa). On the other hand, a strongly textured structure results in significant anisotropy in the alloy, with limited dislocation slip paths and poor high-temperature plastic deformability, ultimately leading to low plasticity (elongation of approximately 5.5% and reduction of area of approximately 12%).

As $Mo_{eq}$ increases, the solid solution content of β-stabilizing elements such as Mo, Nb, Ta, and W rises significantly, producing a strong drag effect at the α/β phase boundary. This causes the width of the α lamellae to narrow substantially from approximately 2.85 μm to less than 1.43 μm, while disrupting the oriented growth pattern of the α phase. As a result, the texture strength weakens, and the texture transitions from an obvious basal-plane texture to a nearly random texture. Polygon diagram data indicate that the texture peaks in high-$Mo_{eq}$ alloys disperse from sharp, point-like features into a uniform distribution, with the α/β phase orientation tending toward isotropy, forming a densely interwoven, multi-directional and basket-weave structure. In the high $Mo_{eq}$ range, the β-phase content increases significantly while the α-phase volume fraction decreases; at the same time, the grain boundary slip effect of the soft β-phase at high temperatures intensifies, causing the tensile strength to decrease linearly (from 580 MPa to approximately 520 MPa). For plasticity, the weakening of texture and the refinement of α-strips form a three-dimensional, interlaced dislocation-blocking network. The multidirectionally interlaced α-strips effectively deflect high-temperature cracks and alleviate stress concentration, while the improvement in isotropy significantly reduces the variability in plasticity data, ultimately increasing the elongation after fracture from approximately 5.5% to a maximum of 15%, thereby achieving a substantial enhancement in high-temperature plasticity.

## 4 Conclusions

Ti-Al-Sn-Zr-Mo-Nb-Ta-W-Si alloy samples were prepared using a vacuum induction suspension melting furnace, and the fluidity property, microstructure, and mechanical properties were investigated. The major conclusions are as follows:

(1) The viscosity of an alloy is the primary factor affecting its casting fluidity. The lower the viscosity, the better the casting fluidity of the alloy. In addition, heat capacity is another important factor, a higher heat capacity corresponds to superior casting fluidity.

(2) With the addition of $Mo_{eq}$ from 0.86 to 4.48, the α-laths are progressively refined, the width of α-laths varies from 2.85 μm to 1.43 μm, and the overall texture intensity exhibits a fluctuating downward trend.

(3) Compared with other alloys, thanks to its minimum viscosity and maximum work hardening rate, Ti-5.76Al-2.30Sn-5.91Zr-3.10Mo-2.94Nb-1.16Ta-0.23Si alloy exhibits the higher fluidity, strength, and elongation.

## Acknowledgments

This work was supported by the Combined Fund of Liaoning, China (Grant No. 2023-MSLH-335) and the Natural Science Found of Shenyang, China (Grant No. 22315605).

## Conflict of interest

The authors declare that they have no known competing financial interests or personal relationships that could have appeared to influence the work reported in this paper.

# References

[1] Uwanyuze R S, Kanyo J E, Myrick S F, et al. A review on alpha case formation and modeling of mass transfer during investment casting of titanium alloys. Journal of Alloys and Compounds, 2021, 865: 158558.
[2] Mahashabde A, Wolfe P, Ashok A, et al. Assessing the environmental impacts of aircraft noise and emissions. Progress in Aerospace Sciences, 2011, 47(1): 15–52.
[3] Jia W J, Zeng W D, Zhou Y G, et al. High-temperature deformation behavior of Ti60 titanium alloy. Materials Science and Engineering: A, 2011, 528(12): 4068–4074.
[4] Yue K, Liu J R, Zhang H J, et al. Precipitates and alloying elements distribution in near α titanium alloy Ti65. Journal of Materials Science & Technology, 2020, 36(1): 93–98.
[5] Fu B G, Wang H W, Zou C M, et al. The effects of Nb content on microstructure and fracture behavior of near α titanium alloys. Materials & Design, 2015, 66: 267–273.
[6] Fu B G, Wang H W, Zou C M, et al. The influence of Zr content on microstructure and precipitation of silicide in as-cast near α titanium alloys. Materials Characterization, 2015, 99: 17–24.
[7] Jiang B B, Wen D H, Wang Q, et al. Design of near-α Ti alloys via a cluster formula approach and their high-temperature oxidation resistance. Journal of Materials Science & Technology, 2019, 35(6): 1008–1016.
[8] Wu X G, Zhang B W, Zhang Y H, et al. Effects of W alloying and heating on microstructure and mechanical properties of a PM Ti-6Al-2Sn-4Zr-2Mo-0.1Si alloy for high temperature applications. Journal of Alloys and Compounds, 2023, 942: 168966.
[9] Narayana P L, Kim S W, Hong J K, et al. Tensile properties of a newly developed high-temperature titanium alloy at room temperature and 650 °C. Materials Science and Engineering: A, 2018, 718: 287–291.
[10] Zhao M Y, Song X Y, Zhang W J, et al. Microstructure and mechanical properties of a novel Ti-6.5Al-2Sn-4Zr-1.5Mo-2Nb-0.25Fe-0.2Si high-temperature titanium alloy. Materials Science Forum, 2020, 993: 351–357.
[11] Jayaprakash M, Ping D H, and Mitarai Y Y. Effect of Zr and Si addition on high temperature mechanical properties of near-α Ti-Al-Zr-Sn based alloys. Materials Science and Engineering: A, 2014, 612: 456–461.
[12] Jiang B B, Wang Q, Wen D H, et al. Effect of Nb and Zr on structural stabilities of Ti-Mo-Sn-based alloys with low modulus. Materials Science and Engineering: A, 2017, 687: 1–7.
[13] Jiang B B, Wen D H, Wang Q, et al. Design of near-α Ti alloys via a cluster formula approach and their high-temperature oxidation resistance. Journal of Materials Science & Technology, 2019, 35(6): 1008–1016.
[14] Zhu Z H, Wang C Y, Liu T Y, et al. Design of ultra-strong as-cast titanium alloy at 600 °C by using cluster formula. Acta Metallurgica Sinica (English Letters), 2024, 37: 2068–2082.
[15] Mehjabeen A, Xu W, Qiu D, et al. Redefining the β-phase stability in Ti-Nb-Zr alloys for alloy design and microstructural prediction. JOM, 2018, 70(10): 2254–2259.
[16] Saha R L and Jacob K T. Casting of titanium alloy and its alloys. Defence Science Journal, 1986, 36(2): 121–141.
[17] Kurz W and Fisher D J. Fundamentals of solidification. 4th revised ed. Trans. Tech. Publications Ltd., 2005.
[18] Devaraj A, Joshi V V, Srivastava A, et al. A low-cost hierarchical nanostructured beta-titanium alloy with high strength. Nature Communications, 2016, 7: 11176.
[19] Liu T Y, Zhu Z H, Zhang S, et al. Design for Ti-Al-V-Mo-Nb alloys for laser additive manufacturing based on a cluster model and on their microstructure and properties. China Foundry, 2021, 18(4): 424–432.
[20] Liu T Y, Liu H Y, Yao Q, et al. Microstructure and mechanical properties of laser additive manufactured novel titanium alloy after heat treatment. China Foundry, 2021, 18(6): 574–580.